Novel position reconstruction methods for highly granular electromagnetic calorimeters

Brendon Madison[1,*] and *Graham* Wilson[1]

[1]Department of Physics and Astronomy, University of Kansas, Lawrence, KS 66045, USA

Abstract. We present work on design and reconstruction methods for sampling electromagnetic calorimeters with emphasis on highly granular designs. We use the clustered logarithmically weighted center-of-gravity estimator (lwk-means) for initial benchmarking of position resolution. We find that the θ and ϕ resolution for high energy photons in Si-W designs improves when increasing both sampling frequency and sampling thickness. Augmenting only one is found to have mixed results. We find that lwk-means is unable to effectively use calorimeter transverse cell sizes smaller than 2 mm. New reconstruction methods for highly granular designs are developed. We find that methods that only measure the initial particle shower and disregard the remaining shower can take advantage of cell sizes down to at least 10 μm, significantly outperforming the benchmark method. Of these, the best method and design is the initial particle shower "single hit" method using the calorimeter design with the highest sampling frequency and sampling fraction.

1 Introduction

We have been working on a new approach to forward calorimetry for luminosity measurement at a future high energy e^+e^- collider using both small-angle Bhabha scattering and the $e^+e^- \rightarrow \gamma\gamma$ process. Improving angular measurements of Bhabhas and $\gamma\gamma$ is important for luminosity systematics, with knowledge of the inner edge of the polar angle acceptance to 10 μrad needed for the 10^{-4} luminosity precision goal with $\gamma\gamma$ [1]. Measurement of $\gamma\gamma$ is also important for addressing beam biases present in Bhabhas. This has focused our attention on how well one can reconstruct high energy electromagnetic showers and in particular those of high energy photons using dedicated electromagnetic calorimeters (ECALs). This application emphasizes high performance energy resolution, polar angle resolution, and azimuthal angle resolution. In the present work, the focus is on position/angle resolution.

In ECAL design, designs that are highly segmented longitudinally typically have high values of Molière radius (R_{M}), corresponding to the lateral spread of an electromagnetic shower being large. This metric is used as a rule-of-thumb for determining the likely quality of position or angle reconstruction of a calorimeter design [2]. It is considered inversely correlated to position/angle resolution. However, as we shall demonstrate in Sect. 3 and Sect. 4, the ultimate position/angle resolution is more related to how well one can construct the interactions associated with the initial shower components.

---

[*] e-mail: brendon_madison@ku.edu

The Molière radius is measured with respect to the shower axis, which is the center-of-gravity (CoG) of the shower along the direction the shower proceeds. In a sandwich calorimeter, with square cells, there is measurement bias in the CoG that arises when the shower is at an angle with respect to the surface of the calorimeter. For this reason it is necessary to measure the particle shower angle before the CoG as the calorimeter measurements must be rotated to correct for this bias. A demonstration of this can be seen in figure 1, wherein the CoG bias from angles of incidence of the particle shower has been simulated for a toy detector concept.

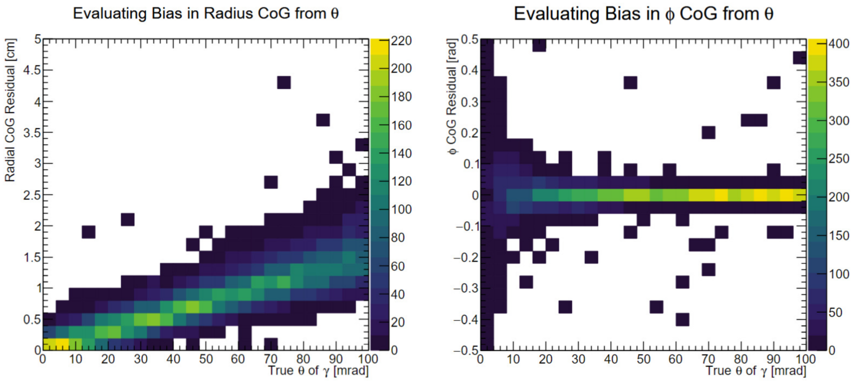

Figure 1. Center-of-gravity bias in radius and ϕ measurements given various values of θ and using 128 GeV photons. This detector simulation was done with a detector displacement from the initial particle position of 2.5 meters. The simulation includes a 3.5T magnetic field. The detector is a sandwich design with cells in the x-y plane and layers along the z-axis.

We observe the expected bias in that the bias in radius for small angles scales linearly with θ and that there is no bias in ϕ with respect to θ. We observe that the ϕ resolution scales with $1/\theta$ (really $1/R$) while the R resolution is constant in θ.

Originally the Molière radius was characterized by the cylindrical radius, about the shower axis, which contains 90% of the deposited energy of the particle shower [3]. The Molière radius can span large values for various experiments, where SiW (Silicon-Tungsten) sandwich can be close to the R_{M} of Tungsten of 9.33 mm while air shower experiments are near 73.3 m. For ECALs made of mixtures of materials the Molière radius can be computed with respect to the electromagnetic scale energy (E_{s}), numerically 21.2 MeV, as

$$R_{\mathrm{M}} = E_{\mathrm{s}} \left[\sum_j \frac{w_j E_{\mathrm{c}}^j}{X_0^j} \right]^{-1} = \left[\sum_j \frac{w_j}{R_{\mathrm{M}}^j} \right]^{-1} \tag{1}$$

where each material is weighted by its fraction by mass, w_j, and using the electron critical energy E_{c}^j and radiation length X_0^j of the material [4]. Note that equation 1 must be computed using the areal density form of X_0^j and R_{M}^j with units of mass/area not the length form.

We can compare R_{M} of two different calorimeter designs by using equation 1. We compare two candidate forward calorimeters, the International Large Detector (ILD) Luminosity Calorimeter (LumiCal) and a work-in-progress proposed new forward calorimeter. This work-in-progress will have 240 layers of $\frac{1}{6}X_0$ SiW , with 1 mm thick silicon. LumiCal uses

30 layers of $1X_0$ SiW, with 0.3 mm thick silicon. For simplicity, we evaluate both of these as square calorimeters, that is to say segmented uniformly in the x-axis and y-axis. We note that the ILD LumiCal is segmented in r-ϕ, into layers of “towers” [5].

Using equation 1 we find that the Molière radius of the ILD Lumical is 14.6 mm while the proposed design is 37.8 mm using assumptions of 1mm PCB and 1mm air gaps. The former is different from the measured “effective” value of 9.46 mm used in the LumiCal reference for a small test-beam setup.

2 Benchmark estimators

2.1 Center of gravity

As established in Sect. 1, to best use methods like CoG or clustering one must remove any angular bias. To remove angular bias one may use angular, i.e. θ or ϕ, CoG. This is often accented by the use of clustering.

The standard CoG method is, mathematically, an average spanning the members of that space. E.g. the CoG for hits along the x-axis is simply the average value of hits along the x-axis. If the CoG is weighted, say by energy, then the user scales the x-axis according to the hit energies and then computes the energy weighted average.

From the standard or energy weighted CoG we can extend to the log-weighted CoG. Previous work has shown that it is less biased and has better resolution for laterally segmented detectors [6]. Here we write the general form of log-weighted weights as

$$w_j = \max\left[0\,, W_0 + \log\left(\frac{w_j^{\mathrm{ini}} x_j}{\sum_j w_j^{\mathrm{ini}}}\right)\right] \tag{2}$$

with dependence on a free parameter W_0, that is to be determined later. The initial weights of equation 2, w_j^{ini}, are determined by the user. The parameter W_0, when using the general form of equation 2, acts as a cut on the initial weights. When W_0 is small, or correspondingly the value of $\sum_j w_j^{\mathrm{ini}}$ is large compared to the average value of w_j^{ini}, hits are given zero weight. Meaning that they are disregarded in the average. This can prove to be problematic in the limit of a large number of hits and low variance in the hit weights where the W_0 parameter will also become a cut on the number of allowed hits.

Typically the hit energy, E_j, is used for w_j^{ini} and the weights of equation 2. Therefore the log-weighted energetic CoG is slightly more complicated than linear weighting. The value of W_0 in equation 2 acts both as a cut on the number of allowed weighted hits and as an energy threshold since energetic weights in equation 2 couple the number and energies of hits with their final weights.

2.2 Clustering

A common clustering algorithm is the k-means algorithm. It is attractive as it is simple and fast. K-means relies on random number generation, and so is sometimes disfavored over concerns that it does not generate exactly reproducible solutions or that this randomness cannot handle complex data. Despite these concerns, extensive studies have shown that k-means reliably converges to optimal solutions within less than 100 iterations outside of special circumstances [7]. Considering this, and that the data here does not meet any referenced circumstances, we find no reason to be concerned with using k-means here [7].

As part of the k-means algorithm, the distance between a hit and all of possible hits is computed. This is done to determine which hits to cluster and which hits to add to which

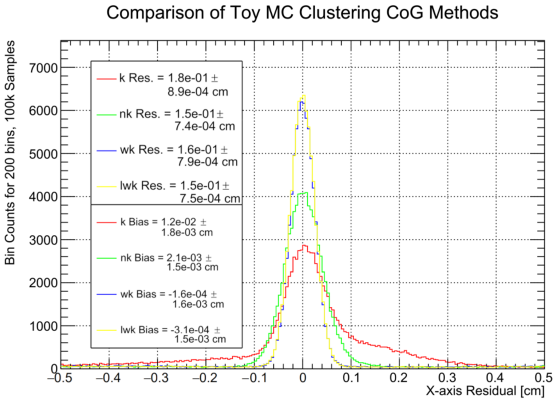

Figure 2. Results for the x-axis residuals for various combinations of clustering and CoG methods. This was done using the toy MC as described in Subsect. 2.2. For conciseness each combination label has been shortened such that k-means is k, nk-means is nk, wk-means is wk and, lwk-means is lwk.

cluster. When dealing with two dimensional data with identical range and variance there is no bias in k-means clustering. Generally, these two constraints are not true and thus there is bias in the k-means clustering [8]. To remedy this, normalized k-means, known as n-k-means, is used [8]. The normalization is done according to range, and not integral, so the range of values lies within [0, 1].

K-means computes centroids, i.e. averages, for clusters during assigning hits to clusters. Centroids are typically computed using an unweighted averaging, i.e. an unweighted CoG method as done in Subsect. 2.1. We may expand the k-means CoG to use weighted methods such that we have weighted k-means, wk-means, and log-weighted k-means, lwk-means.

We test the combinations of these different CoG approaches and clustering. The experimental approach is to use a toy MC. We simulate three clusters that are chosen about the circumference of a circle that is centered in x,y at (0,0). So that the average of the clusters should give (0,0). The radius of the circle is chosen by a uniform random number from a value from 1 cm to 3 cm. Then three angles are chosen for the clusters such that they have equal angular separations of $\frac{2\pi}{3}$ radians. Then 72 hits are generated, with 12 for the first cluster, 24 for the second cluster and 36 for the third cluster. This is done purely for testing the algorithm, not for reasons relevant to electromagnetic particle showers. Each cluster is also given a different variance in spatial distribution that is consistent across each trial of the simulation. Each hit is given a Gaussian weighting, to simulate energy weighting, that is maximal at the center of the cluster. The y-axis values are also scaled by a factor of three to simulate the reality that the clustering axes may not be similar in scale. After this, the position values were set to the centers of 100 micron cells. This simulation was then run for 100k trials.

To evaluate resolution the single axis resolution was computed from the residual of the CoG of the clusters with respect to the origin. We then numerically evaluate the resolution using the central 95.5% interquantile range (IQR) of the residuals (corresponding to $\pm 2\sigma$ for a Gaussian). This robust estimate is then rescaled by $\frac{1}{2}$ to be a consistent estimate of the $\pm 1\sigma$ resolution. The bias is evaluated using the median of the residuals.

As seen in figure 2 for the x-axis resolution, lwk-means performs best in resolution, roughly 10% better than wk-means and that both are unbiased. This result also finds that the resolution is larger than the intrinsic resolution expected from cell size. So there is a need to find better methods in order to reach the intrinsic resolution.

3 Results for chosen benchmark estimator

Following the results of Sect. 2.2, and the results of other sources, we have chosen to use lwk-means as the benchmark for this section [6]. For testing this method we have simulated, in GEANT4, four designs. Two $1X_0$ designs and two $\frac{1}{6}X_0$ designs. Each design is simulated with both a silicon thickness of 0.3 mm and 1 mm. The simulation was done with fixed angles of θ of 50 mrad and ϕ of $\frac{\pi}{4}$. We chose not to use test beam geometry, where the angles are set to zero, as the bias observed in figure 1 shows that this case would be poorly representative of typical function. The initial particle was chosen to be a 128 GeV γ so that these results can be applied to future studies of $\gamma\gamma$ luminosity studies at various energies that are spaced according to $\log_2(E)$. The materials used in the detector were a passive layer of tungsten, an active layer of silicon, 1 mm of PCB (G10) and 1 mm of air gap. The detector was offset longitudinally from the beam origin by 2.5m in order to be comparable to the ILD forward calorimeter region [9].

This is done with numerous values of different cell sizes for the silicon active layer. Digitization is done after GEANT4 is run such that the generator level information of the steps in GEANT4 are stored and then digitized afterwards based on the specifications of the cells that the user wants. This was done to avoid geometry limit issues and memory issues that can arise in GEANT4 when one tries to simulate numerous layers of small, $\leq$100 μm, cells. There is also a possibility of charge sharing but the work shown here does not include any charge sharing of nearby pixels.

For this particular simulation, since there are no “towers” as there are in the ILD LumiCal design, instead the initial clustering is done in layers [5]. As in the ILD LumiCal reconstruction, clustering is then repeated in these segments, again here layers instead of “towers”, and then repeated across layers until there is one centroid. This centroid, i.e. final CoG, is then treated as the measurement. We also use the same optimized value of $W_0 = 3.4$ as is done elsewhere [6].

Investigating the results of figures 3 and 4, we may model the change in performance for a given detector design, using a CoG approach such as in this section, as follows. We propose that the position resolution

$$\sigma_{\text{pos}} \sim \frac{R_{\text{M}}^{\text{L}}}{\sqrt{f_{\text{samp.}}}\,\mathcal{N}^{\frac{1}{4}}} \tag{3}$$

depends on the Molière radius, in units of length, the sampling frequency, $\mathcal{N}$, and the sampling fraction, $f_{\text{samp.}}$, which is unitless. This model is not entirely original as calorimeter design references note the dependence on Molière radius and sampling fraction [10]. The addition of dependence on sampling frequency is motivated by the fact that increased sampling frequency results in additional measurements of the particle shower.

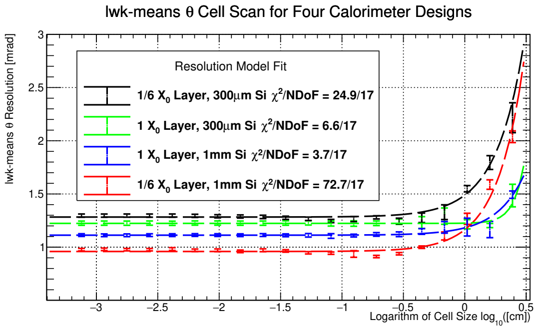

Figure 3. Results of cell scan of θ resolution using four calorimeter designs to use as reference. The estimator used is the log-weighted k-means, lwk-means, method. We observe that the designs with thicker silicon are superior for θ resolution. The fit corresponds to a parameterized form of equation 5.

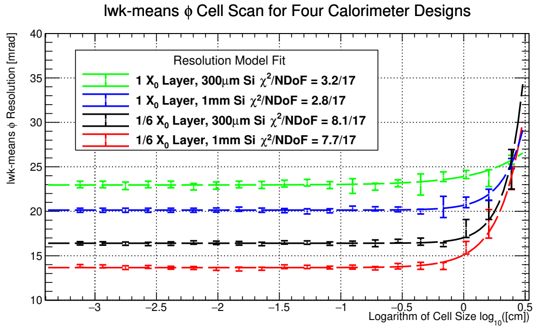

Figure 4. Results of cell scan of ϕ resolution using four calorimeter designs. The reconstruction method used is the log-weighted k-means, lwk-means, method. We observe that designs with higher sampling frequency are superior for ϕ resolution. The fit corresponds to a parameterized form of equation 5.

We can also relate the sampling fraction to the thickness of the active component and passive component [10]. The sampling fraction is defined by

$$f_{\rm samp} = \frac{E_{\rm act.}}{E_{\rm act.} + E_{\rm pas.}} \approx \frac{dE_{\rm act.}}{dx} d_{\rm act.} \left[\frac{dE_{\rm act.}}{dx} d_{\rm act.} + \frac{dE_{\rm pas.}}{dx} d_{\rm pas.} \right]^{-1} \tag{4}$$

and thus depends on the energy deposited in the active and passive layers. This is typically done by choosing a specific physics process, namely MIPs [10]. For said physics process there is a known energy per length differential of dE/dx which typically varies for different materials and thus the different notation for the active and passive materials. Values for the electromagnetic energy fraction in the active material for the tested calorimeter designs can be seen in table 1. The values of energy resolution were found to scale with the expected trend of $1/\sqrt{f_{\rm samp.}}$ [10]. Deviations from this trend, comparable to 10%, were observed for the $\frac{1}{6}$ X_0 with 300 μm and 1 X_0 with 1 mm designs. It is expected that effects from changes in energy sampling between designs, such as characterized by the e/mip ratio, can influence this trend [10]. Still, it was found that the e/mip ratio was not sufficient to explain the deviations. Further testing is needed to determine the source of these deviations.

We can expand equation 3 further, to include effects from transverse cell size, $d_{\rm cell}$, as has been shown in previous work [11]. Thus equation 3 is rewritten to

$$\sigma_{\rm pos} \sim \frac{R_{\rm M}^{\rm L}}{\sqrt{f_{\rm samp.}} \mathcal{N}^{\frac{1}{4}}} \oplus e^{d_{\rm cell}} \tag{5}$$

which has an exponential dependence on cell size[1]. This term is added in quadrature such that, for methods or designs that become limited by other factors, smaller cell sizes do not improve performance. This exponential trend in cell size is observed as a linear trend in the log plots of figures 3 and 4.

For fitting the cell scan plots seen in figures 3 and 4 we use a parameterized form of equation 5

$$\sigma_{\rm pos} \sim \sigma_0 \oplus a_0 e^{a_1 (d_{\rm cell} - a_2)} \tag{6}$$

which uses a constant, minimal, position resolution of σ_0 and then three parameters of a_0, a_1 and, a_2 for manipulating the exponential term. Using equation 6 leads to plausible fit qualities for the 1 X_0 designs but questionable ones for the $\frac{1}{6}X_0$ designs for the θ dependence (Fig. 3). Particularly the fit of the $\frac{1}{6}X_0$ designs are poor around the 5 mm cell size area.

To address the poor quality of fit for the $\frac{1}{6}X_0$ designs we propose

$$\sigma_{pos.} \sim \sigma_0 \oplus \left(a_0 e^{a_1 (d_{\rm cell} - a_2)} + a_3 e^{a_4 (d_{\rm cell} - a_5)^2} \right) \tag{7}$$

---

[1] The argument of the exponential function is unitless, being of the form $d/d_{\rm ref}$.

Table 1. A selection of the four electromagnetic calorimeter designs with measured electromagnetic deposited energy fractions and energy resolution for 128 GeV photons. All calorimeters are sufficiently deep to guarantee excellent longitudinal containment (here $40X_0$.)

Energy Resolution			
Layer Design	Si Thickness [mm]	EM Fraction	Energy Resolution
$1\ X_0$	0.3	0.964%	$18.4\%/\sqrt{E}$
$1\ X_0$	1	3.31%	$15.7\%/\sqrt{E}$
$\frac{1}{6}\ X_0$	0.3	5.21%	$6.6\%/\sqrt{E}$
$\frac{1}{6}\ X_0$	1	17.0%	$4.8\%/\sqrt{E}$

an exponential expansion of the cell size dependent term. We repeat the fitting process as done before in figure 3 with the updated model of equation 7. During the evaluation of fits, seen in figure 5, it was determined that the additional factor of equation 7 influences the resolution by roughly 0.2%. To better assess the fit of equation 7 one needs considerable increase in data precision. Given these results equation 7 is a plausible model for position resolution when incident particle energy is fixed and one only varies sampling frequency and sampling fraction.

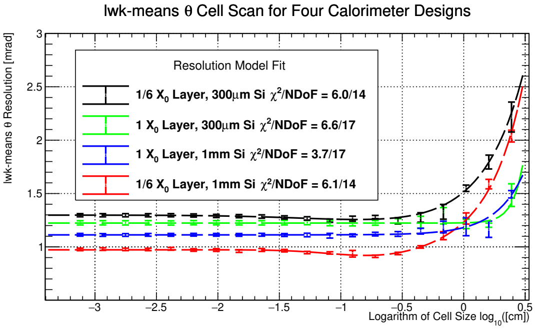

Figure 5. Following figure 3, we repeat the cell size scan of θ for the new model of equation 7 for the $\frac{1}{6}X_0$ designs. The new model brings the quality of fits to being comparable to previous fits for $1\ X_0$ designs. Only the $\frac{1}{6}X_0$ design fits differ from Fig. 3.

To determine how well a pairing of calorimeter design and reconstruction technique does at exploiting the transverse cell size being used, we introduce $d_{\min}$, the minimum cell size. The implementation of $d_{\min}$ here uses a 1% threshold of the minimum of the fit of the cell scan resolution. This is done to account for possible diminishing returns that may persist as transverse cell size is made smaller. Knowing the value of the minimum cell size for a particular pairing allows for constraining the calorimeter design in terms of transverse cell size. It also may serve as a communication tool for comparing the resolution of similar designs and reconstruction methods.

The minimum cell size values were found using the fits seen in figures 4 and 5 and then compiled into table 2. This table also features the minimum resolution values as found using the lwk-means method with the various designs. Examining the resolution and minimum cell size values reveals that there is no shared ordering for the designs. Increasing both sampling frequency and sampling fraction simultaneously, as done in the $\frac{1}{6}X_0$ and 1 mm silicon design, was observed to have benefits for improving both metrics for both angles. The $\frac{1}{6}X_0$ and 1 mm silicon design was also found to be the best design for position resolution in both angles.

The results of table 2 also indicate that the cell size does not have significant effect on lwk-means reconstruction below 2 mm in cell size. As such, lwk-means reconstruction is not desirable in circumstances where one wishes to use smaller cell sizes to achieve higher resolution. Lwk-means reconstruction is suitable for large cell sizes where it is able to ap-

Table 2. Extrapolated minimum cell size given the fits seen in figures 4 and 5. Values are calculated using the fits of said figures. These results are representative of their listed designs and the lwk-means reconstruction method.

Minimum Cell Size for lwk-means Reconstruction			
Design	Variable	Resolution [mrad]	Minimum Cell Size (d_{min}) [mm]
1 X_0 , 0.3 mm Si	θ	1.22 ± 0.01	9.2 ± 0.8
1 X_0 , 1 mm Si	θ	1.11 ± 0.01	3.5± 0.4
$\frac{1}{6}$ X_0 , 0.3 mm Si	θ	1.30 ± 0.01	2.1 ± 0.2
$\frac{1}{6}$ X_0 , 1 mm Si	θ	0.98 ± 0.01	1.8 ± 0.2
1 X_0 , 0.3 mm Si	ϕ	23.0 ± 0.2	9.3 ± 0.8
1 X_0 , 1 mm Si	ϕ	20.1 ± 0.2	6.5 ± 0.7
$\frac{1}{6}$ X_0 , 0.3 mm Si	ϕ	16.5 ± 0.2	4.8 ± 0.5
$\frac{1}{6}$ X_0 , 1 mm Si	ϕ	13.7 ± 0.2	4.0 ± 0.4

proach the $\frac{d}{\sqrt{12}}$ fundamental geometric cell resolution limit. We can test this by noting that the geometric cell resolution limit for θ

$$\sigma_\theta = \frac{d}{z_{\text{offset}}\sqrt{12}} \tag{8}$$

depends on the transverse cell size, d, and the offset of the calorimeter from the interaction point along the z-axis, z_{offset}. As an example, for the $\frac{1}{6}X_0$ and 1 mm silicon design equation 8 would be roughly 0.6 mrad. Which is slightly smaller than the value of 0.98 mrad observed in table 2.

We warrant the result of lwk-means reconstruction with three conditions. Other cell designs, such as $r\phi$ cells, can be used and they may be more advantageous for lwk-means. The lwk-means method also has numerous parameters that can be further tuned for these particular designs, which was not exhaustively done here. In addition to this algorithmic tuning it is common to have weights for layers, both depending on the shower shape and quality of the layer's measurement, such as done in OPAL's luminosity measurement [12].

3.1 Projecting results

Given the results of Sect. 3, the GEANT4 simulations and the resolution models provide a starting point for further extrapolation for the purpose of determining optimal calorimeter design. Using equation 3 and equation 4 one can project an expected relative spatial resolution is, assuming ideal reconstruction and ignoring effects of transverse cell size.

The results were expressed relative to the values from the 1 X_0 and 0.3 mm silicon design. This projection was given three constraints for possible projected designs with particular emphasis on constraining to a design that is feasible for the forward calorimeter region of ILD [9]. Designs that exceed 1 m in total length are excluded to respect the space of the forward calorimeter region [9]. The maximum cell thickness was constrained to 1.8 mm in order to keep possible designs within ranges that have been experimentally tested in other work [13].

The results, as seen in figure 6, indicate that the ordering and magnitudes of resolutions, as seen in table 2, are not consistent with the projection. However, it is not expected for the ordering or magnitude of this projection to match as this projection includes only calorimeter design effects and no reconstruction effects.

Considering the results of this projection it is clear that more granular designs are preferred for improving position resolution. The design that uses $\frac{1}{6}X_0$ and 1 mm silicon is not

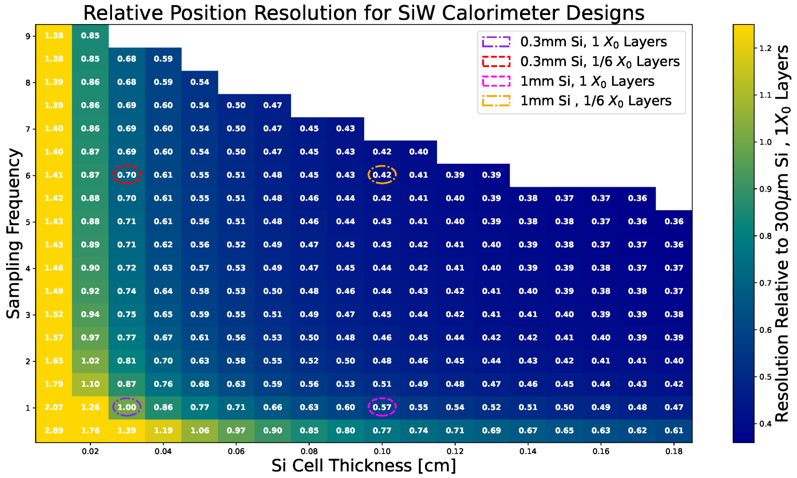

Figure 6. Results of extrapolating equation 3 with its two parameters. The sampling frequency scales with the plot y-axis while the sampling fraction is related to the sampling thickness. Four points are marked for reference as the designs being tested in this work. In each case there are 1mm thick G10 and air layers.

only the best design tested here but performs near the optimal point of the projected designs. Since the performance of the lwk-means reconstruction seen in Sect. 3 does not agree with the significantly better performance for granular designs seen in figure 6, we suspect that new methods, particularly suited for granular designs, need to be developed. To do so we must investigate things that granular designs are suited for.

4 New reconstruction proposal

In a calorimeter designed for tracking the sampling frequency is typically increased compared to calorimeters built for energy resolution where the sampling fraction would be increased instead. The increased sampling frequency allows for numerous measurements to be made of incoming particles with minimal scattering of the incoming particle. We propose to mimic this process for highly granular sampling calorimeter designs by focusing on the initial part of the particle shower. In this regime the shower is not well described by the Molière radius, so we do not expect large values of Molière radius to degrade performance. Instead the shower is characterized by the spread of the photon conversion that starts the particle shower. This is characterized by the physics of the Bethe-Heitler process where the opening angle is quite narrow, $\approx 1/\gamma = m_e/E_\gamma$, and inversely related to the incident photon energy [14]. For an incident 128 GeV photon, as used in the GEANT4 simulations done here, this corresponds to 4.0 μrad.

4.1 Investigating the initial shower

If we investigate the first five radiation lengths of the particle shower, such as in figure 7, we can see that the structure of the initial shower, and its trajectory, are much clearer in the more granular design. There are numerous layers where the only hits within the window displayed in figure 7 are the ones from the initial shower conversion. The increased number of samples, by virtue of increased sampling frequency, allows for the use of more comprehensive methods like averaging and fitting. The increased number of samples also inherently reduces the statistical error. There are thus multiple reasons to believe that the granular design can outperform the low sampling frequency design on position resolution.

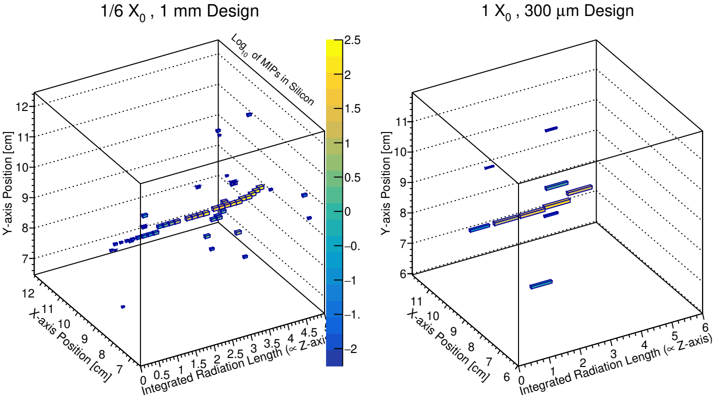

Figure 7. Event display comparing the initial shower for two different events for two different designs. The first five radiation lengths of layers after the shower start are shown for each. Both are 128 GeV γ events that converted in tungsten, have the same incident angles, and are centered on the conversion point along the x-axis and y-axis positions. The transverse cell sized used for both was 100 μm but the bin sizes are 10 times this, at 1 mm. The plots share one color axis that represents the energy in each bin as the logarithm of the number of MIPs. The integrated radiation length is relative to the conversion point.

4.2 New methods

To begin testing methods of position reconstruction using only the initial particle shower we have chosen to isolate the initial particle shower from the remaining shower. To do this, a window is used in terms of the z-axis, or layer number, and the value of θ corresponding to hits in the active layer with respect to the interaction point. We have chosen not to use any windowing in ϕ for this study. Since we anticipate varying the cell size, as done in Sect. 3, we need to choose a value for the θ window that will be small enough to take advantage of the cell size. As such, we have fixed the value of θ for the window to be the equivalent angular spread of three transverse cell sizes, centered on the cell the shower starts in.

In this study we wanted to mainly be sensitive to the underlying calorimeter design and not systematics from the reconstruction method. As such we have “cheated” the values for the true angles of θ and ϕ as well as the position of the start of the electromagnetic shower. By cheating these values we ensure that the windowing is being utilized correctly.

The windowing process starts with applying the cut in θ centered on the true θ value. This windowing cut was scaled according to the transverse cell size such that it would be a three cells in diameter. The remaining hits are then discarded if they exist outside the window. A second cut is applied to exclude hits that occur deeper than the layer with maximum energy deposit. Of the remaining hits an algorithm, which starts at the earliest hit along the z-axis, checks the subsequent layer for hits. If there are no hits then the algorithm assumes that the initial shower has scattered out of the window and truncates the sample to those which are before this point. If there are hits in the next layer then it includes these hits with the starting hit and then repeats the process, looking at the next layer for hits. This repeats until either no new hits are found in the window or the layer of the shower maximum is reached. At this point the algorithm stops and the collected hits are used as representing the initial shower.

The efficiency of this windowing algorithm, done with the four different designs, can be seen in figure 8. We find that, regardless of which design is used, there are a significant number of events that fail to have any hits within the window. An exception to this is a sweet-spot for both granular, $\frac{1}{6}X_0$ layers, designs around the 100 micron transverse cell size. We postulate that this sweet-spot occurs because the equivalent angular spread per layer for these cell sizes approaches 1–10 microradians. This angular spread is similar to the spread expected from either multiple scattering or photon conversion [4] [15]. Due to these sources of angular spread, cells that are even smaller end up with particles of the initial shower not being in the same cell or even being nearest neighbors. Therefore a windowing algorithm that cuts out beyond nearest neighbors, as done here, is cutting out some of the particles of the initial shower. This suggests that the windowing algorithm needs improvement to handle these other cases. Similar to the results for position resolution in Sect. 3, the best design for window efficiency is almost always the $\frac{1}{6}X_0$ and 1 mm silicon design.

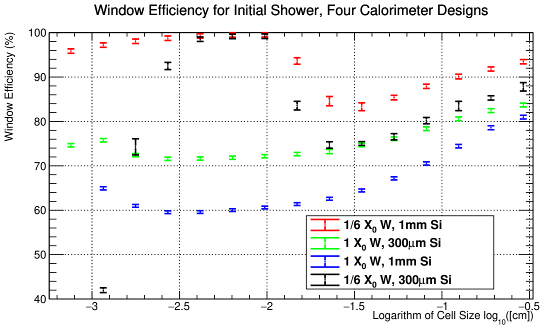

Figure 8. Window efficiency for θ window used for the initial shower reconstruction methods. Events where there are no hits in the silicon within the window after the start of the shower cause the less than 100% efficiency.

Inspired by other work that fits electromagnetic showers, we chose to test both averaging and fitting of the initial particle shower [16]. Both averaging and fitting were tested using unweighted and energy weighted versions. It was found that averaging always resulted in a slightly poorer resolution to fitting. As such we do not present the results of using the averaging reconstruction methods. For notation purposes, we refer to the unweighted initial shower fit method as the IS fit and the energetically weighted initial shower fit method as the ISE fit.

Fitting was done by fitting the θ of the windowed hits to a single parameter of a constant. This was done so that the quality of fit, and the uncertainty of the fitted value, could be used in analysis. The results of the fitted reconstruction methods, as seen in figures 9, have similar linear trends in the log-log plots of resolution and cell size. This is indicative of the exponential term seen in equation 5.

Unlike the results of Sect. 3 we do not see evidence of a minimum resolution being reached all the way down to the smallest, roughly 10 μm, cell size tested here. Instead the fitting methods seem to follow the geometric value of $d/\sqrt{12}$. This indicates that these reconstruction methods are well suited to future designs that seek to exploit smaller cell sizes. Comparing the two fit methods against each other we find that the unweighted fit performs slightly better. We also observe that the best design is the $\frac{1}{6}X_0$ and 1 mm silicon design.

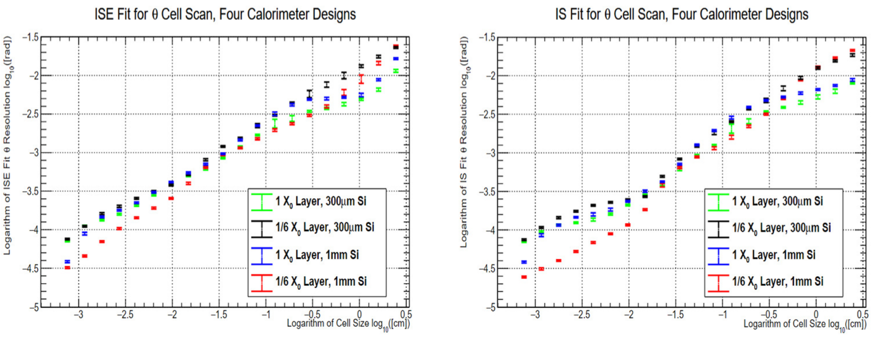

Figure 9. Results of cell scan of θ resolution for the ISE fit (left), the unweighted initial shower fit method, and the IS fit (right), the energy weighted initial shower fit method. At cell sizes smaller than 100 microns the $\frac{1}{6}X_0$ and 1 mm silicon design is best. Similar performance is observed for both methods.

For the sake of comparison of the fit methods we chose to restrict to 100 micron transverse cell size and use the best design. For 100 micron cells the best design is the $\frac{1}{6}X_0$ and 1 mm design. At this point, the IS θ fit has a resolution of 0.10 ± 0.01 mrad and the ISE θ fit has a resolution of 0.22 ± 0.01 mrad. So the unweighted fit outperforms the energy weighted fit by about a factor of two. It should be expected that weighting for energy in the initial shower does not improve performance as it makes the reconstruction sensitive to the particle multiplicity of the initial photon conversion as well as fluctuations in the energy depositions.

As an alternative to the fitting methods we propose a new approach that assumes that we have a method of determining which hit in the initial shower sample has the minimum residual to the true θ value. This method, dubbed the “single hit” method due to it relying on a single hit, uses cheated information so that the method can be evaluated without systematics of the method used in the identification of the single hit. The result of the single hit method, as seen in figure 10, has a significantly different trend from those seen in Sect.3 or for the previous fitting methods.

We observe that the performance of the single hit method is superior to the previous fit methods with a minimum resolution in θ of 2.95 ± 0.05 micro-radians. As discussed in Sect. 4, this is similar to the order of magnitude expected for the initial shower. Figure 10 also shows that, for ϕ resolution, the single hit method can approach 0.1 mrad resolution. The performance is best for the 1 mm Si with $1/6\ X_0$ layers design around 100 micron transverse cell size. We postulate that this optimal point occurs for similar angular spread reasons that were observed with window efficiency in figure 8. This performance surpasses even the value expected from the geometric limit computed from equation 8. While this is initially unexpected there is a plausible explanation. The single hit method requires sampling numerous points. When the incidence angle of the incident particle is non-zero there is a significant chance that the shower, as it travels through multiple layers, will hit cells that are not perfectly aligned. This staggering in the cells results in

$$d_{\mathrm{eff}} = \frac{d}{N_{\mathrm{IS}}} \tag{9}$$

an effective cell size we refer to as d_{eff}. This effective cell size can be reduced by as much as the number of layers in the initial shower, here written as N_{IS}. This staggering can be observed in figure 7, where there are multiple bins in the second layer on the granular calorimeter’s

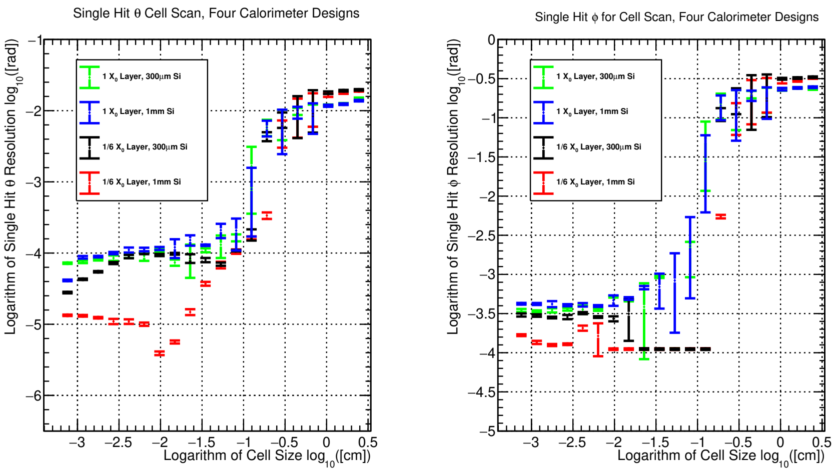

Figure 10. Results of cell scan of θ and ϕ resolutions for the single hit method. At cell size of roughly 100 microns the $\frac{1}{6}X_0$ and 1 mm silicon design is best.

event display. We note that equation 9 assumes that the spacing of layers can optimally take advantage of this staggering effect, which is likely not true. Still, this is a plausible explanation as choosing a single hit bypasses the averaging that gives rise to the typical limit seen in equation 8.

For the single hit method to be viable in an un-cheated analysis a method for identifying the minimum residual hit is needed. More work needs to be done to better understand the staggering effect and how it affects the methods covered in this section.

5 Conclusion and outlook

Related to further studies on forward calorimeter design at future high energy e^+e^- colliders, this work has displayed numerous benefits for calorimeter designs with higher sampling frequency and higher sampling thicknesses. Of all the reconstruction methods tested here, the $\frac{1}{6}X_0$ and 1 mm silicon design, which had both the maximally tested sampling frequency and sampling thickness, outperformed the other designs in both θ and ϕ resolution. This design is also, per our projections of possible calorimeter designs presented in Sect. 3.1, within the forward calorimetry space constraint for future linear colliders and close to optimal position resolution. Our new reconstruction methods, covered in Sect. 4, are capable of approaching, and even surpassing, the typical geometric resolution limit for cell sizes down to, at least, 100 μm. We expect that a staggering effect, which yields a smaller effective cell size, is responsible for the minimum θ resolution for the single hit method of 2.95 ± 0.05 micro-radians. Further work needs to be done to flesh out the new reconstruction methods: both in terms of improving the windowing process and in terms of making the analysis a purely detector level analysis.

6 Acknowledgements

This work is partially supported by the US National Science Foundation (NSF) under awards NSF 2013007 and NSF 2310030 and benefited from use of the HPC facilities operated by the Center for Research Computing at the University of Kansas supported in part through the NSF MRI Award 2117449.

References

[1] G. Wilson and B. Madison, "Reimagining e^+e^- collider precision luminosity measurements", these proceedings (2024).

[2] K. Greisen, "Cosmic Ray Showers". Annual Review of Nuclear Science. 10. Laboratory of Nuclear Studies, Cornell University, Ithaca, N. Y.: 71. (1960) https://doi.org/10.1146/annurev.ns.10.120160.000431

[3] N. R. Walter, et al., "Electron-Induced Cascade Showers in Copper and Lead at 1 GeV". Physical review Vol. 149, Pages 201-208 (1966). http://doi.org/10.1103/PhysRev.149.201

[4] D.E. Groom, S. R. Klein for P.A. Zyla et al. (Particle Data Group), Prog. Theor. Exp. Phys. 2020, 083C01 2021 update (2021).

[5] I. Levy, "Detector R&D towards realistic luminosity measurement at the forward region of future e^+e^- linear colliders". Thesis submitted to Tel Aviv University (2019). https://inspirehep.net/files/5a22206735eb2ffe0e97f5e36d128080

[6] T.C. Awes, et al., "A Simple method of shower localization and identification in laterally segmented calorimeters" , Nucl. Instrum. Meth. A Vol 311 Pages 130-138 , (1992) https://doi.org/10.1016/0168-9002(92)90858-2

[7] A. Broder, et al., "Scalable K-Means by Ranked Retrieval" , WSDM'14 (2014) http://dx.doi.org/10.1145/2556195.2556260

[8] D. Virmani, S. Taneja, G. Malhotra, "Normalization based K means Clustering Algorithm" , IJAERS , arxiv[cs.LG]:1503.00900 , (2015) https://doi.org/10.48550/arXiv.1503.00900

[9] H. Abramowicz, et al., "International Large Detector: Interim Design Report" , (2020) https://doi.org/10.48550/arXiv.2003.01116

[10] R. Wigmans, *Calorimetry Energy Measurement in Particle Physics*, 2nd Edition, Oxford Science Publications, Oxford 2017.

[11] F. Binon, et al., "HODOSCOPE GAMMA SPECTROMETER GAMS-200" , Nucl. Instrum. Meth. , Vol 188 Pages 507 (1981) https://doi.org/10.1016/0029-554X(81)90261-5

[12] G.Abbiendi, et al., "Precision Luminosity for Z0 Lineshape Measurements with a Silicon-Tungsten Calorimeter" , Eur.Phys.J.C14 Pages 373-425, (2000) https://doi.org/10.1007/s100520000353

[13] B. F. Philips, et al., "Development of thick intrinsic silicon detectors for hard X-ray and gamma-ray detection" , IEEE , (2001) https://doi.org/10.1109/NSSMIC.2001.1008442

[14] H. Bethe and W. Heitler, "On the Stopping of Fast Particles and on the Creation of Positive Electrons" , Proceedings of the Royal Society of London. Series A, Containing Papers of a Mathematical and Physical Character Vol. 146, No. 856 , pp. 83-112 , (1934) https://www.jstor.org/stable/2935479

[15] G. R. Lynch, O. I. Dahl, "Approximations to multiple Coulomb scattering" , Nuclear Instruments and Methods in Physics Research Section B: Beam Interactions with Materials and Atoms, Volume 58, Issue 1, 2 May 1991, Pages 6-10 (1991) https://doi.org/10.1016/0168-583X(91)95671-Y

[16] G. Grindhammer, S. Peters, "The Parameterized Simulation of Electromagnetic Showers in Homogeneous and Sampling Calorimeters" , Proceedings of Int. Conf. on Monte Carlo Simulation in High Energy and Nuclear Physics, Tallahassee, Florida, USA, (1993) https://doi.org/10.48550/arXiv.hep-ex/0001020